Supplementary Materials

Operando study of the influence of small molecule acceptor on the morphology induced device degradation of organic solar cells with different π-π stacking

Xinyu Jiang[1,†], Alexander J. Gillett[2,†], Tianle Zheng[1,3], Xin Song[4,5], Julian E. Heger[1], Kun Sun[1], Lukas V. Spanier[1], Renjun Guo[1], Suzhe Liang[1], Sigrid Bernstorff[6], Peter Müller-Buschbaum[1,7*]

[1] Technical University of Munich, TUM School of Natural Sciences, Department of Physics, Chair for Functional Materials, James-Franck-Str. 1, 85748 Garching, Germany

[2] Cavendish Laboratory, University of Cambridge, JJ Thomson Avenue, Cambridge, U.K.

[3] Department of Chemistry, College of Sciences. Shanghai University, 200444, Shanghai, P. R. China

[4] School of Materials Science and Engineering, Jiangsu Engineering Laboratory of Light-Electricity-Heat, Energy-Converting Materials and Applications, Changzhou University, Changzhou 213164, P. R. China

[5] Key Laboratory of Advanced Energy Materials Chemistry (Ministry of Education), Nankai University, Tianjin 300071, China

[6] Elettra-Sincrotrone Trieste S.C.p.A., Strada Statale 14 km 163.5, AREA Science Park, Basovizza, 34149 Trieste, Italy

[7] Heinz Maier-Leibnitz Zentrum (MLZ), Technical University of Munich, Lichtenbergstr. 1, 85748 Garching, Germany

* Email: muellerb@ph.tum.de

[†] These authors contributed equally to this work.

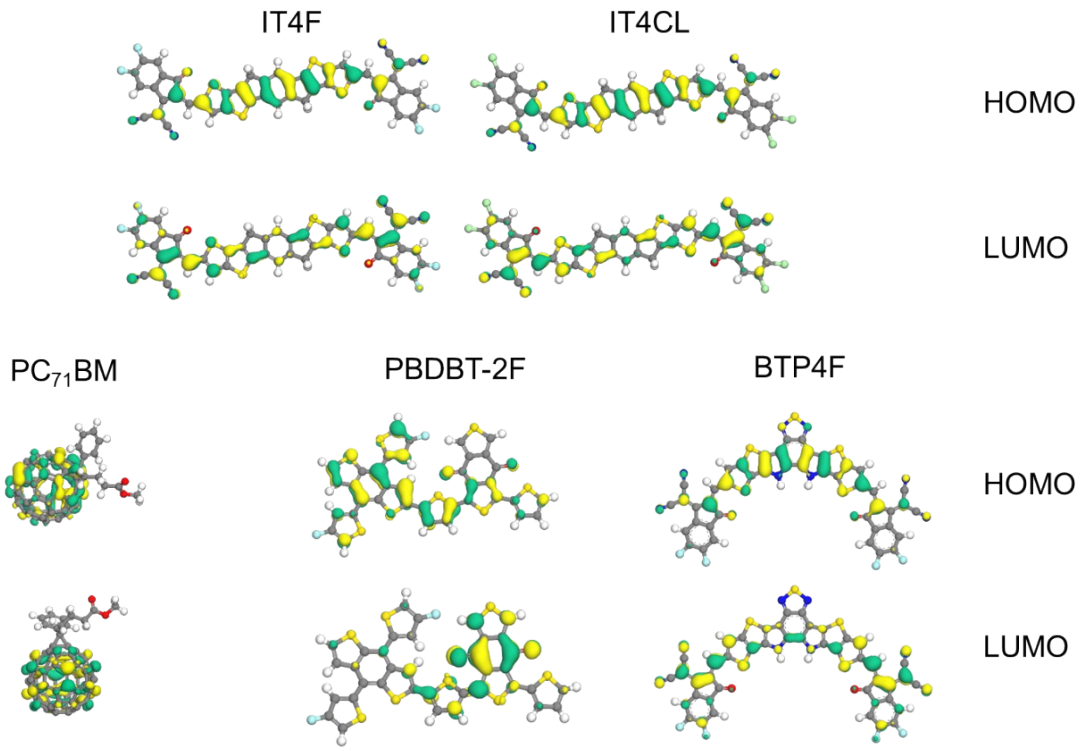

Fig. S1. Calculation of the HOMO and LUMO levels of the polymer donor and acceptor molecules used in the present study.

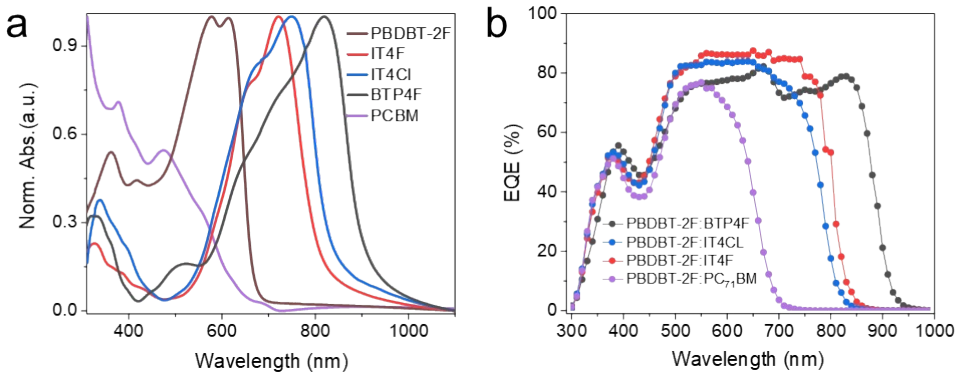

Fig. S2. **a.** Normalized UV-Vis spectroscopy data of the neat films of the donor and acceptors used in this work. **b.** EQE of the OSCs based on PBDBT-2F with different acceptors.

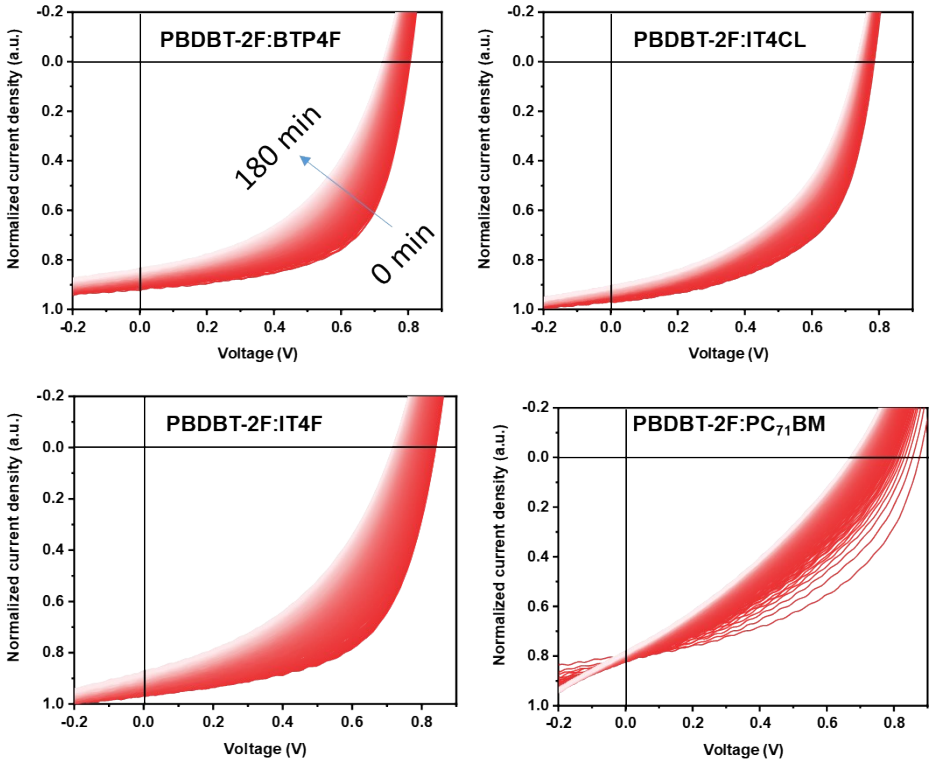

Fig. S3. Recorded current–voltage curves (with normalized initial short-circuit current density) as a function of time for devices based on different active layers as indicated in the legend during the operando experiments.

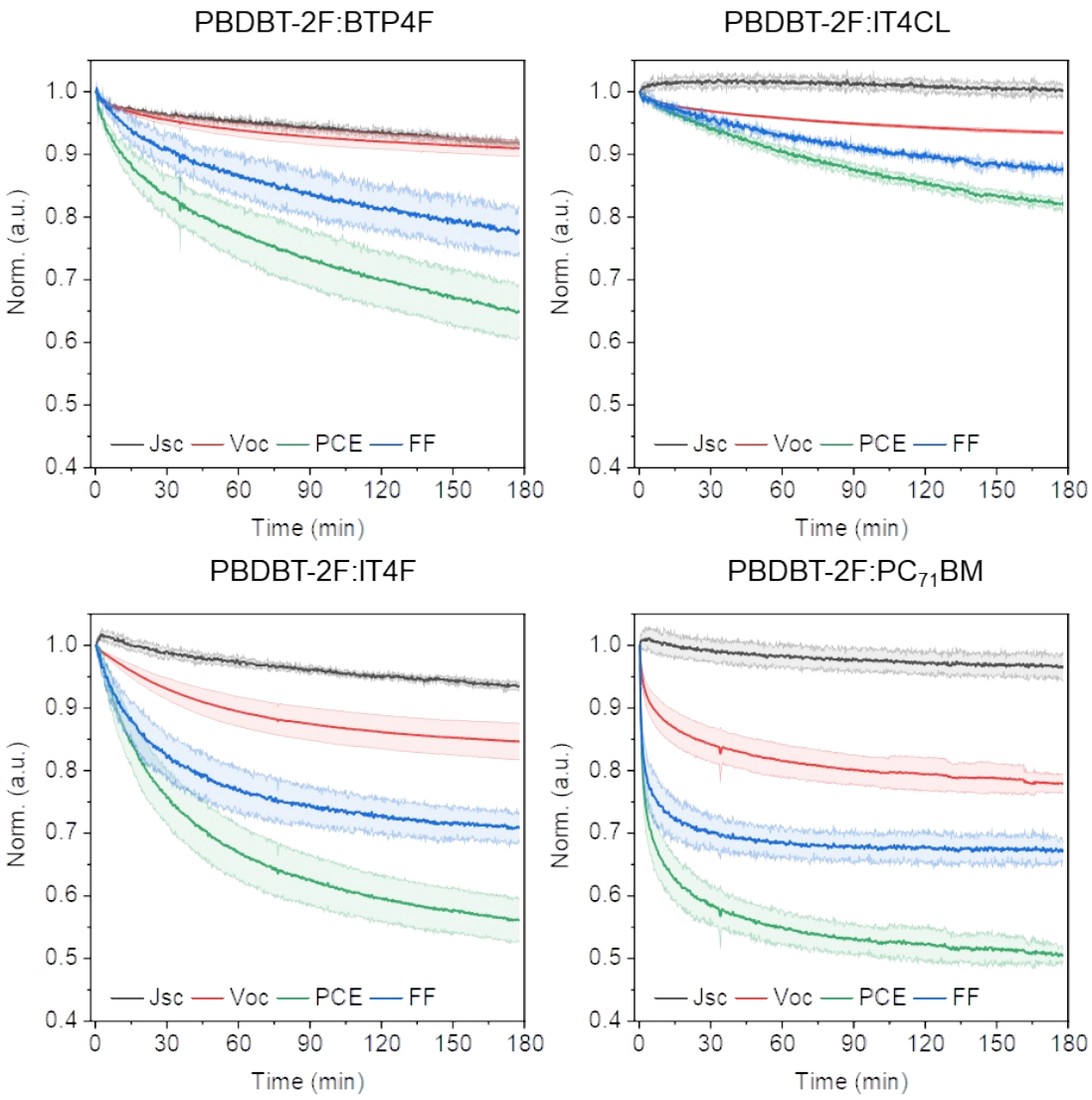

Fig. S4. Time evolution of the photovoltaic characteristics (Jsc in black, Voc in red, FF in blue and PCE in green) of each OSC type, normalized to their initial values for the sake of clarity.

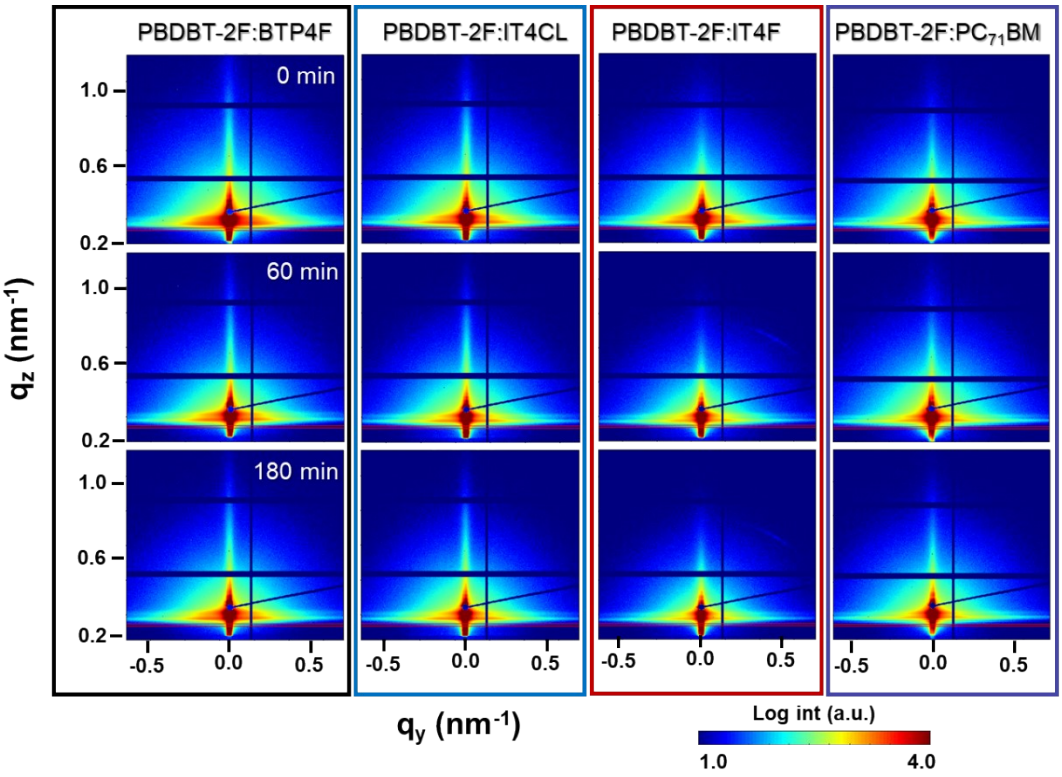

Fig. S5. Selected 2D GISAXS data measured during the operando experiments as a function of time for devices based on different active layers as indicated in the legend.

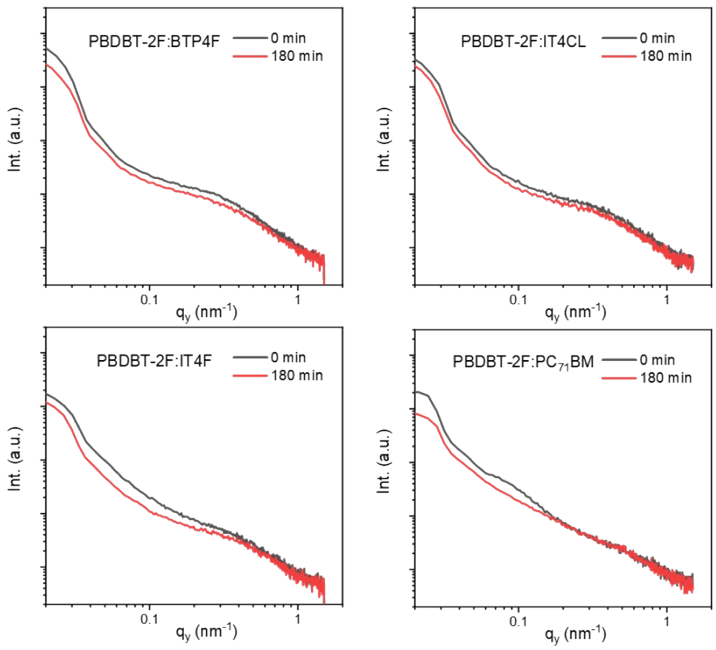

Fig. S6. Comparison of horizontal line cuts of the 2D GISAXS data taken at the critical angle of the active layer before (0 min) and after (180 min) the operando measurements.

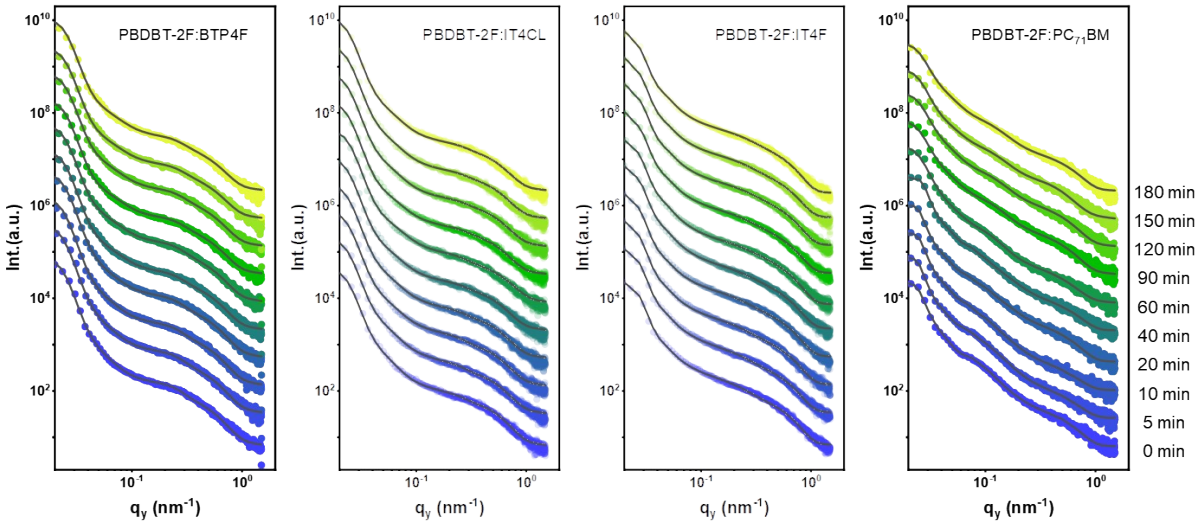

Fig. S7. Horizontal line cuts of the 2D GISAXS data (dots) and corresponding model fits (black lines) from the operando GISAXS measurements at different times as indicated. The curves are shifted along the y axis for the sake of clarity.

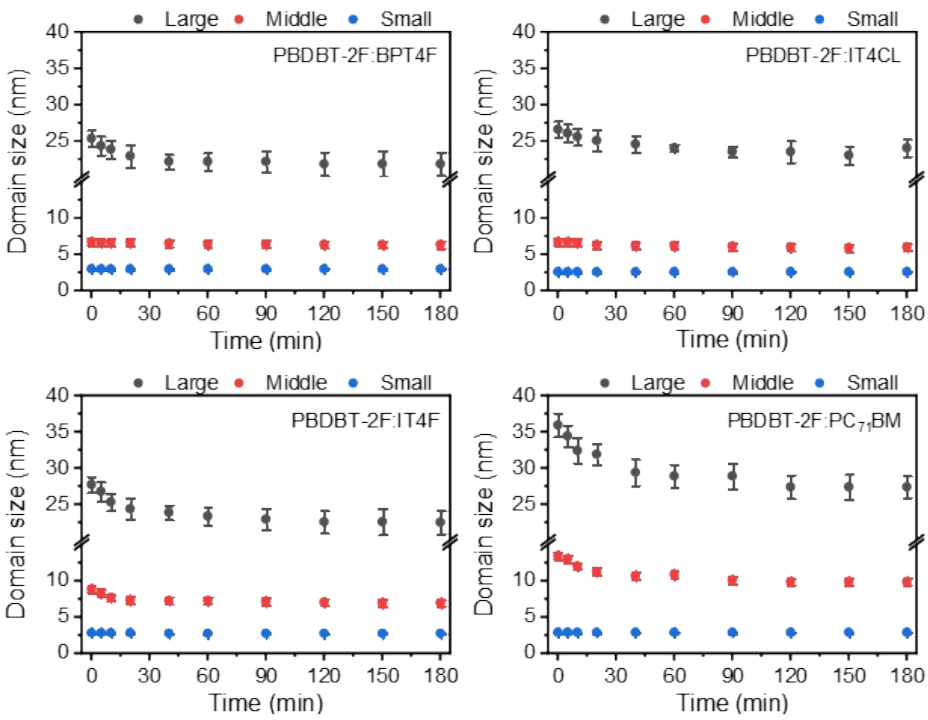

Fig. S8. Temporal evolution of domain radii of large (black) and middle (red) small structures of the active layer extracted with GISAXS modelling of the operando experiments for the different active layer OSCs as indicated.

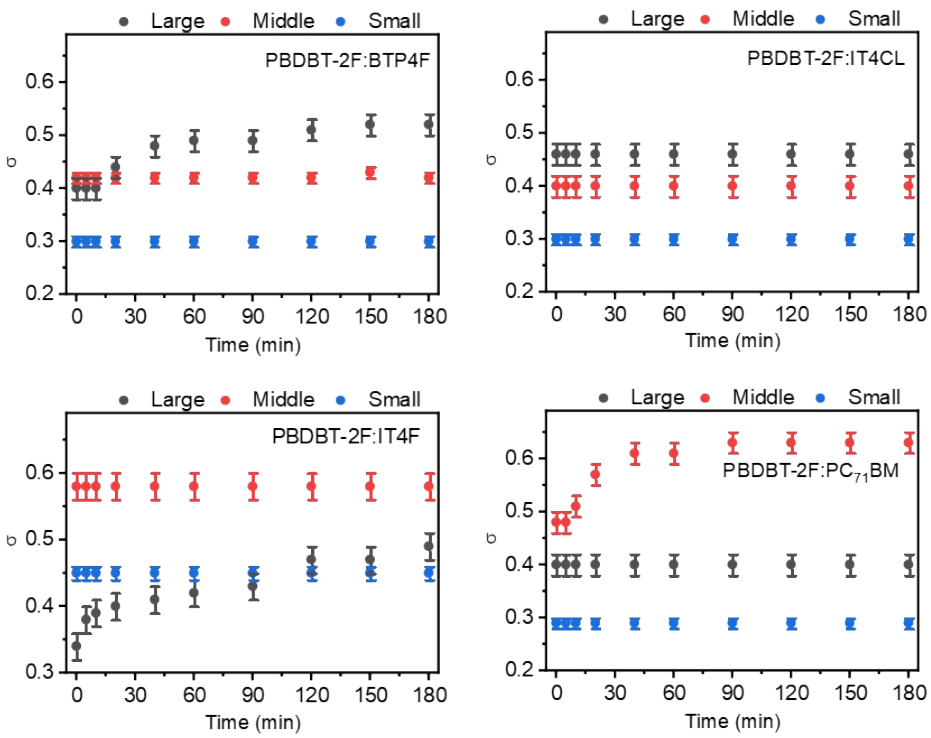

Fig. S9 Temporal evolution of normalized domain radii polydispersity (σ) of the active layer extracted with GISAXS modelling of the operando experiments for the different active layer OSCs as indicated.

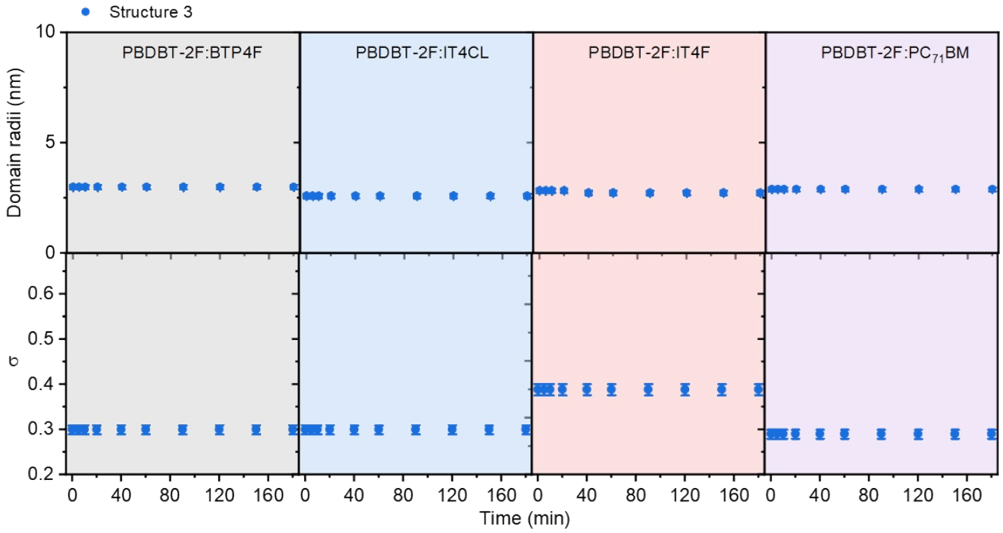

Fig. S10. Temporal evolution of domain radii (structure 3) and the corresponding polydispersity (σ) of the active layer modeled by GISAXS during the operando experiments for the different active layer OSCs as indicated.

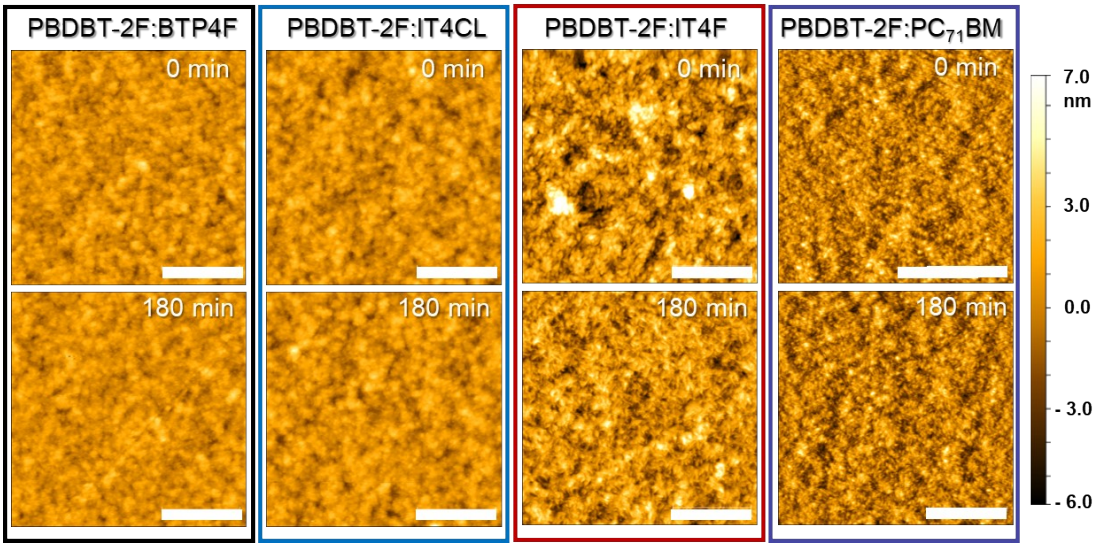

Fig. S11. AFM height images of the active layers based on different accepters before (0 min) and after (180 min) the operando measurements. The insert scale bar denotes 1 µm.

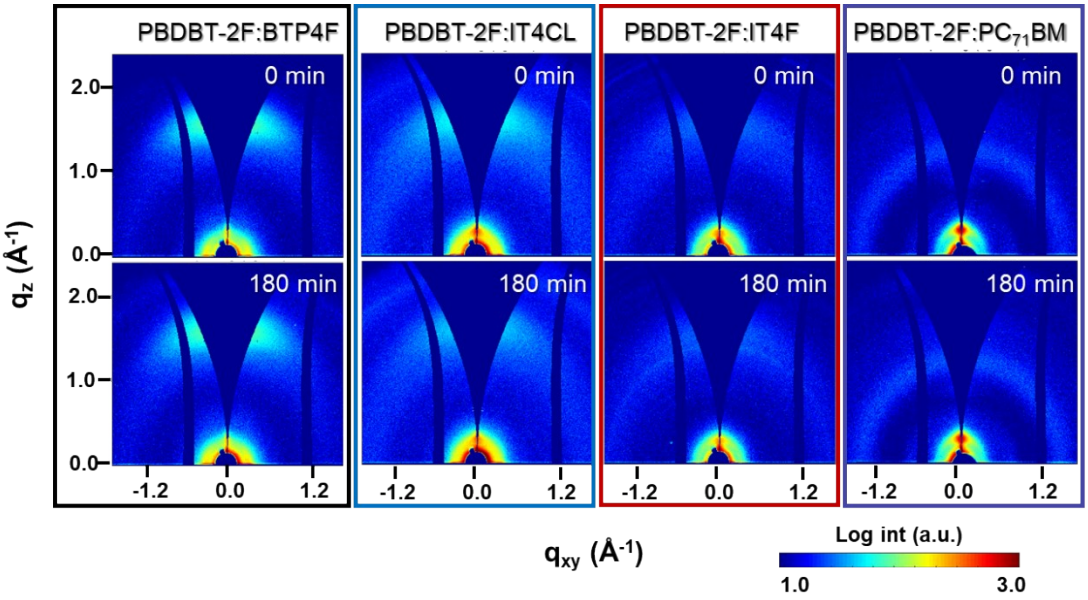

Fig. S12. 2D GIWAXS data of the active layer based on different acceptors before (0 min) and after (180 min) the operando measurements.

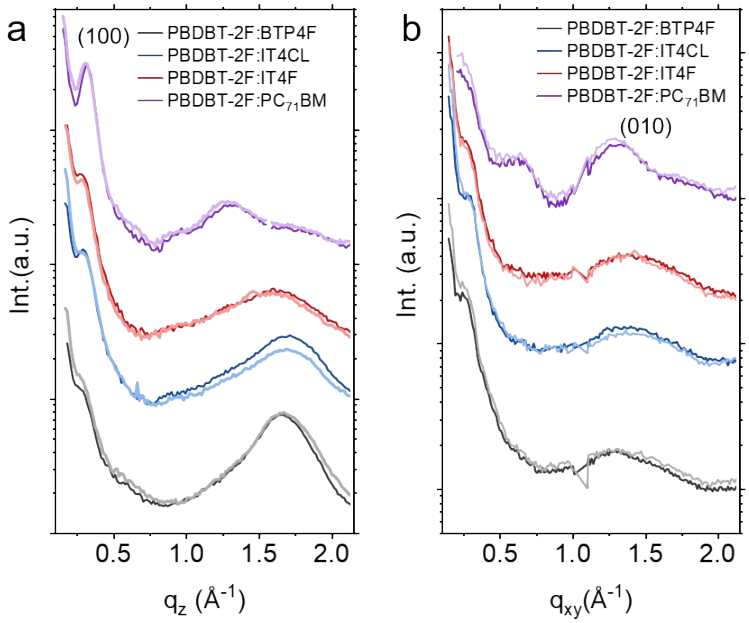

Fig. S13. **a.** Out-of-plane (OOP) and **b.** in-plane (IP) cuts from the 2D GIWAXS data of the active layers based on different accepters before (dark lines) and after (light lines) the operando measurements. The characteristic Bragg peaks are labelled.

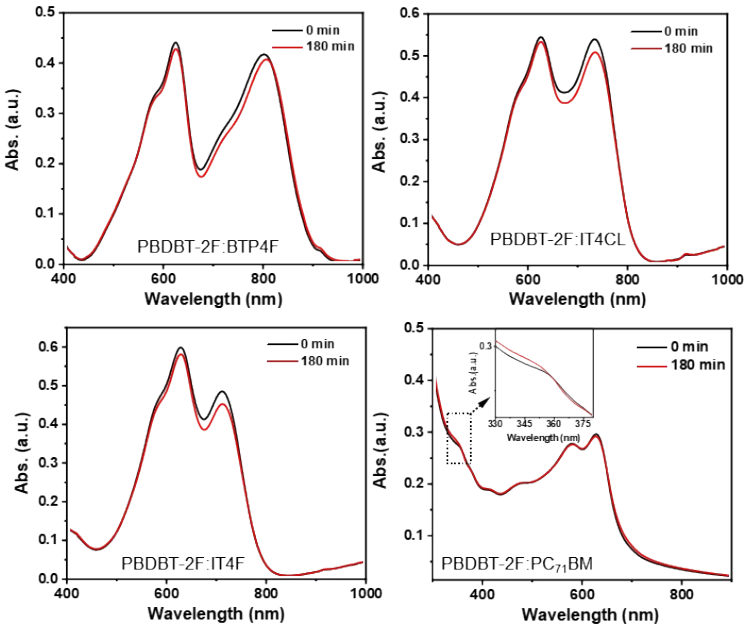

Fig. S14. UV-VIS data of the device based on different accepters before (0 min) and after (180 min) the operando measurements.

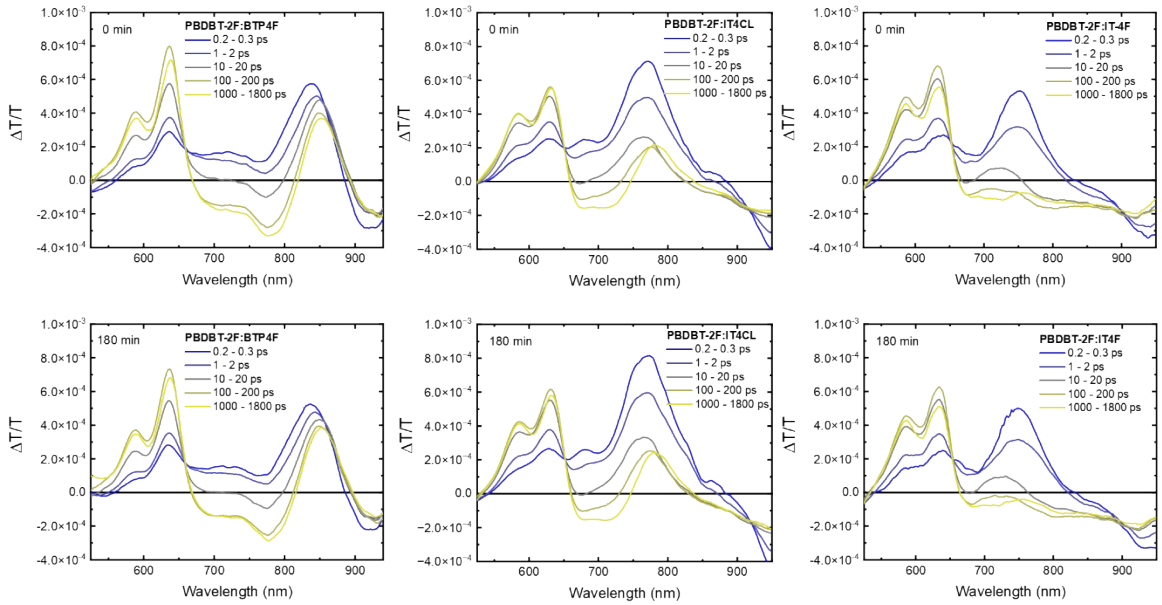

Fig. S15. TA spectra at different time delays for PBDBT-2F:BTP4F (pump at 800 nm for the preferable excitation of BTP4F), PBDBT-2F:IT4CL(pump at 730 nm for the preferable excitation of BTP4F) and PBDBT-2F:IT4F (pump at 730 nm for the preferable excitation of BTP4F) after the operando measurements.

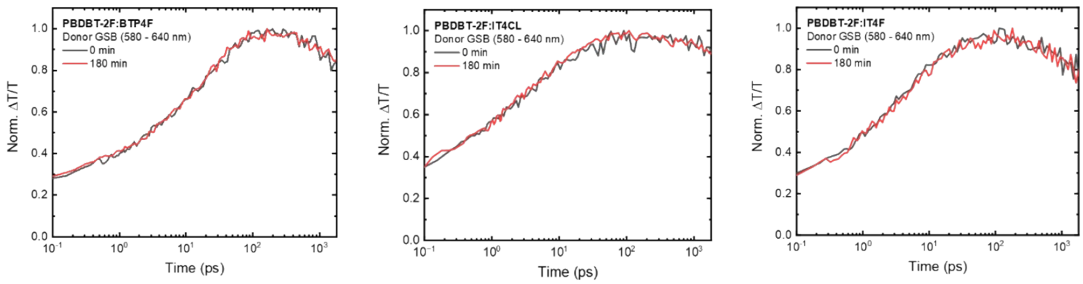

Fig. S16. Kinetics extracted from polymer ground state bleach (GSB) at 580–640 nm for PBDBT-2F: NFAs, i.e. pumping in the acceptor region for a preferable excitation of the NFAs.

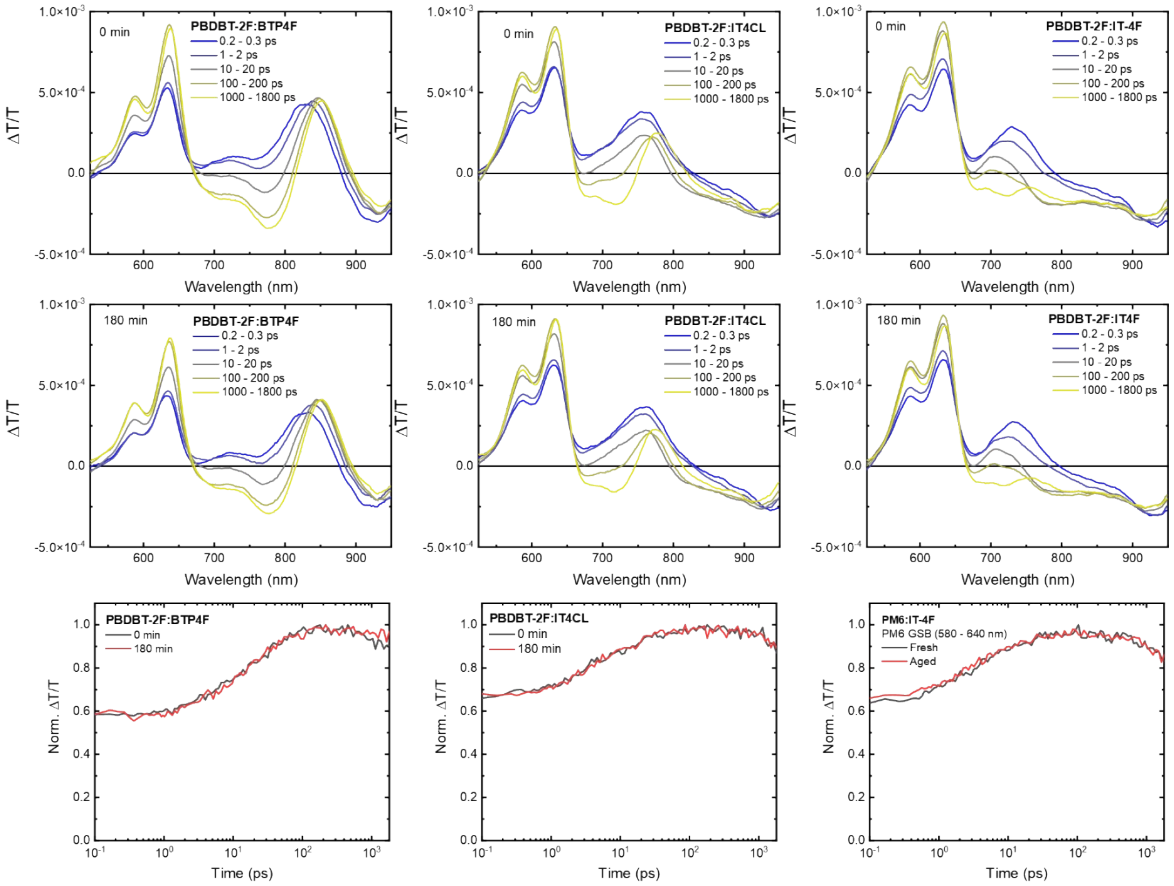

Fig. S17. TA spectra at different time delays and kinetics extracted from polymer ground state bleach (GSB) (580–640 nm) for PBDBT-2F:BTP4F, PBDBT-2F:BTP4CL and PBDBT-2F:IT4F before (0 min) and after (180 min) the operando experiments (pump: 580 nm for the preferable excitation of PBDBT-2F).